RSC Advances

PAPER

View Article Online
View Journal | View Issue

Cite this: *RSC Adv.*, 2025, **15**, 29097

Clinical evaluation of [^{99m}Tc]Tc-PSMA-P1: a promising SPECT radiotracer for prostate cancer imaging

Maria Hassan,[a] Tanveer Hussain Bokhari,*[a] Faiz Ahmed,[a] Yun-Sang Lee[b] and Nadeem Ahmed Lodhi *[c]

This study aimed to design and synthesize a prostate-specific membrane antigen inhibitor (PSMA-P1) and to formulate a freeze-dried kit for radiolabeling with Technetium-99m (^{99m}Tc) to improve prostate cancer detection. A molecular docking study was carried out to calculate affinity parameters against four targeted protein structures (PDB IDs: 2ZCH, 2XW1, 2OOT, and 2XV7) to provide a comprehensive understanding of ligand–receptor interactions, along with structural features of synthesized PSMA to explain their QSAR. PSMA-P1 was efficiently synthesized using solid-phase peptide synthesis (SPPS), which served as the basis for its chemical synthesis. The freeze-dried kit of PSMA-P1 was formulated for the easy preparation of [^{99m}Tc]Tc-PSMA-P1 with high radiochemical purity (≥99%). [^{99m}Tc]Tc-PSMA-P1 showed strong binding affinity (K_i = 69.14 μM) with PDB ID: 2OOT. The [^{99m}Tc]Tc-PSMA-P1 demonstrated high stability (≥95% up to 4 h) *in vitro* in serum, hydrophilicity (log $D_{7.4} = -2.55 \pm 0.130$), and strong PSMA binding affinity ($K_d = 16.14 \pm 1.452$ nM). The accumulation of [^{99m}Tc]Tc-PSMA-P1 (1.68 ± 0.16% ID g^{-1}) was prominently observed at 4 h post-injection in the 22Rv1 tumor model. The co-injection of 2-PMPA significantly inhibited the uptake of [^{99m}Tc]Tc-PSMA-P1 to PSMA-expressing tumors and tissues, indicating that PSMA selectively mediates these uptakes. The SPECT/CT results are consistent with the *in vivo* biodistribution. The first single-patient study further revealed that [^{99m}Tc]Tc-PSMA-P1 is an efficient imaging agent for PSMA-expressing tumors. This will be a promising candidate for prostate cancer.

Received 20th June 2025
Accepted 19th July 2025

DOI: 10.1039/d5ra04397b

rsc.li/rsc-advances

1 Introduction

Prostate cancer is the most common disease in men and the 2nd largest cause of cancer-related mortality.[1] In 2024 nearly 1 466 718 cases of prostate cancer are expected to be diagnosed worldwide, with 299 010 cases likely to originate from the US.[2] The Prostate-specific membrane antigen (PSMA) has emerged as a widely recognized molecular target for visualizing PCa due to its over-expression on PCa cells. PSMA, or glutamate carboxypeptidase II (GCPII), breaks down *N*-acetylaspartylglutamate (NAAG) into *N*-acetylaspartate (NAA) and glutamate through enzymatic hydrolysis. Consequently, GCPII(PSMA) inhibitors could reduce glutamate and elevate NAAG levels.[3] The first PSMA crystal structure was discovered in 2005, and facilitated understanding the basic structure of protein and clarified the significant ligand interactions.[4,5] The entire PSMA cavity surrounding the active site consists of two distinct regions responsible for substrate binding: the S1′ site is more specific to glutamate moieties, however, the S1 site offers more flexibility and preferably accepts lipophilic interactions.[6,7] Initially, a humanized anti-PSMA mAb-J591 demonstrated favorable properties and was labeled with Indium-111 for PSMA imaging.[8] Despite increased target efficiency, it was not suitable because of its larger size, low tumor-to-background contrast, and slow pharmacokinetics making frequent use of antibody-based imaging in nuclear oncology inconvenient.[9]

The Food and Drug Administration (FDA)-approved the first radiotracer for Positron Emitting Tomography (PET) imaging of PCa was [^{68}Ga]Ga-PSMA-11. Gallium-68 is widely available through ^{68}Ge/^{68}Ga generators, eliminating the need for an on-site cyclotron facility. However, challenges may arise due to generator availability, cost, and regulatory constraints in certain centers.[10] In December 2020, the FDA approved [^{18}F]F-DCFPyL (piflufolastat F 18), a fluorine-18 (^{18}F) labeled PSMA-targeted PET imaging agent for prostate cancer.[11] This approval represented a significant step forward, offering advantages over the Gallium-68-based radiotracers, such as a longer half-life ($T_{1/2}$ =

[a]*Department of Chemistry, Government College University, Faisalabad-38000, Pakistan. E-mail: dr.tanveerbokhari@yahoo.com; tanveerhussain@gcuf.edu.pk; Tel: +92-333-3725151*

[b]*Department of Nuclear Medicine, Seoul National University College of Medicine, Seoul, Republic of Korea*

[c]*Isotope Production Division, Pakistan Institute of Nuclear Science & Technology (PINSTECH), P. O. Nilore, 45650, Islamabad, Pakistan. E-mail: nadiimlodhi@gmail.com; Fax: +92-51-9248808; Tel: +92-51-9248769*

110 minutes), which allows for wider distribution to facilities without an on-site cyclotron. Additionally, [18F]F-DCFPyL demonstrates high affinity for PSMA, providing excellent imaging resolution and sensitivity in detecting both primary and metastatic prostate cancer lesions.[12]

Technetium-99m (^{99m}Tc) is widely used in diagnostic imaging because of its favorable physical characteristics (γ = 141 keV with 89% abundance), easy availability (^{99}Mo/^{99m}Tc generators), limited radiation toxicity, excellent coordination chemistry, making it highly suitable for Single Photon Emission Computed Tomography (SPECT/CT) imaging.[13,14] Furthermore, its half-life ($T_{1/2}$ = 6 h) is adequate for ^{99m}Tc radiopharmaceutical preparation in hospitals pharmacy allowing ample time for quality control, administration to patients, and image acquisition.[15,16] Several urea-based small [^{99m}Tc]Tc-PSMA tracers including [^{99m}Tc]Tc-MAS$_3$-y-nal-k(Sub-KuE),[17], [^{99m}Tc]Tc-MIP-1417,[18], [^{99m}Tc]Tc-PSMA I&S,[19], [^{99m}Tc]Tc-MIP-1405,[20] [^{99m}Tc]Tc-MIP-1340 (ref. 21) [^{99m}Tc][Tc]-PSMAT4 (ref. 22) have been clinically evaluated for SPECT/CT imaging of PCa.

[^{99m}Tc]Tc-HYNIC-ALUG has emerged as a valuable imaging agent and demonstrated successful utility in the initial staging of 227 PCa patients.[23] This development also led to creating a freeze-dried kit for [^{99m}Tc]Tc HYNIC-ALUG,[24] simplifying preparation and clinical implementation. However, its pharmacokinetic profile presents certain challenges. Studies have reported high renal uptake and prolonged retention, which may interfere with image interpretation and increase radiation exposure to non-target organs. Furthermore, notable accumulation in the intestines and gallbladder suggests hepatobiliary involvement in excretion, leading to non-ideal clearance patterns. These challenges highlight the need for structural modifications to optimize pharmacokinetics while maintaining high PSMA binding affinity.[25] In this present study, we focus on the *in silico* evaluation and solid phase synthesis of PSMA-P1, incorporating phenyl (Phe) as the linker moiety, and HYNIC as the ligand. This modification was introduced to optimize receptor binding by engaging the hydrophobic pocket within the PSMA S1 site, potentially enhancing affinity and specificity. Additionally, the new molecular structure was designed to reduce renal retention and minimize hepatobiliary excretion, thereby improving imaging performance. Moreover, the lyophilized kit formulation was developed to facilitate the efficient preparation of [^{99m}Tc]Tc-PSMA-P1 at the hospital pharmacy. The targeting potential of [^{99m}Tc]Tc-HYNIC-PSMA-P1 for imaging prostate cancer was evaluated in an animal model. The first patient study further provides the effectiveness of [^{99m}Tc]Tc-PSMA-P1 in the clinical setting.

2 Material and methods

All reagents were of analytical grade and used as received without additional purification. Anhydrous dichloromethane (DCM), dimethylformamide (DMF), *N*,*N*-diisopropylethylamine (DIPEA), methanol, 2CTC (2-chloro-trityl), bis(*t*-Bu)-L-glutamate hydrochloride, tetrakis(triphenyl)palladium (TTPP), triphosgene, diethyldithiocarbamate trihydrate, Fmoc-phenylalanine (Fmoc-phe-OH), 1*H*-1,2,3-benzotriazol-1-ol (HOBT), 2-(1*H*-benzotriazole-1-yl)-1,1,3,3-tetramethylaminium tetrafluoroborate (TBTU), piperidine, 6-aminohexanoic acid, fluorenyl methoxycarbonyl chloride, 6-[2-(*tert*-butoxycarbonyl) hydrazino]nicotinic acid, trifluoroacetic acid (TFA), ethylenediaminediacetic acid (EDDA), tricine, D-mannitol, stannous chloride dehydrate ($SnCl_2 \cdot 2H_2O$) were purchased from Sigma-Aldrich (Germany). 6-Amino-hexanoic acid (Ahx) was synthesized according to reported methods.[26,27] The 22Rv1 human prostate cancer epithelial cell line was procured from the American Type Culture Collection (ATCC). Human serum was obtained PAEC, Nilore Islamabad hospital. [^{99m}Tc]$NaTcO_4$ elution was obtained from the ^{99}Mo/^{99m}Tc generator using saline provided by the Pakistan Institute of Nuclear Science and Technology (PINSTECH). ITLC-SG strips were counted using a Mini-Scan (Eckert & Ziegler, Germany) system. Radio-high performance liquid chromatography (Radio-HPLC) was performed using (HITACHI-Japan, auto-sampler L-2200) integrated with UV detection was performed at 220 nm, along with radioactivity monitoring using a Bioscan system (Japan) equipped with a NaI(Tl) scintillation detector. Semi-prep HPLC was performed on an X-Bridge BEH C_{18} OBD™ 10 mm × 250 mm, 130 Å, 10 μm column (Waters) and analytical HPLC was performed on column (C18) 4.6 mm × 100 mm, 120 Å column (Waters). Proton NMR spectra were recorded on a Bruker Avance II 500 MHz spectrometer, with chemical shifts referenced to TMS (δ = 0 ppm).

2.1 Molecular docking

Molecular docking studies were performed for the designed PSMA-P1 and [^{99m}Tc]Tc-PSMA-P1, as well as with reference compound HYNIC-ALUG and [^{99m}Tc]Tc-HYNIC-ALUG, with four different receptors obtained from protein data bank; human glutamate carboxypeptidase II (PDB ID: 2OOT),[28] human prostate specific antigen (PDB ID: 2ZCH),[29] human serum albumin (PDB ID: 2XW1),[30] vascular endothelial growth factor-D (PDB ID: 2XV7).[31] These simulations were done using docking software the AutoDockTools 4.2 version 1.5.6 (ADT).[32] Molecular interactions for both ligands were visualized using Discovery Studio Visualizer (DSV)[33] software. Ligand and ^{99m}Tc labelled complex structure geometry (Fig. S1 and S2) optimization performed using B3LYP basis sets 6-311G(d,p) to calculate HOMO–LUMO energy gap using Gaussian 16 (ref. 34) and GaussView 6 tools.[35] Quantitative Structure–Activity Relationship (QSAR) calculations were performed with OSIRIS Data Warrior version v06.01.00 (ref. 36) and Molinspiration Cheminformatics calculation of molecular property service[37] was utilized to assess toxicity risk and calculated various molecular parameters.

2.2 Synthesis of PSMA-P1

The solid phase synthesis of PSMA-P1 is shown in Scheme S1. Initially, 2-CTC resin (1.55 mmol, 1 g) was soaked for 30 min in dry DCM (3 mL) followed by the addition of Fmo-Lys (Alloc)-OH (2.8 g, 6.2 mmol), and DIPEA (6 mL, 37 mmol). The reaction mixture was stirred gently for 18 h to produce lysine-immobilized resin **3**. After the completion of the reaction resin was washed with DCM (3 × 20 mL) and unreacted CTC

groups were blocked by reacting it with a mixture of methanol and DIPEA (1 : 1) for 30 min. Fmoc was removed by treating with 10 mL of 20% piperidine in DMF. A solution of bis(*t*-Bu)-L-glutamate hydrochloride (1.8 g, 6.2 mmol) and DIPEA (4 mL, 24 mmol) in anhydrous DCM (90 mL) was mixed to triphosgene (0.6 g, 2.3 mmol) in DCM (30 mL) over a period for 4 h at 0 °C and stirred for 30 min to obtain **5**. Subsequently, lysine immobilized resin (**3**) (1 g, 1.55 mmol) was added at once and the reaction mixture was stirred for 20 hours at room temperature. After the completion of reaction resin was washed with DMF (3 × 10 mL) and DCM (3 × 10 mL) to get **6**. The alloc protecting group was removed by reacting the resin with TTPP (0.5 g, 0.46 mmol) in the presence of morpholine (13.8 mmol, 6.6 mL) in DCM for 3 h in darkness. Washing of the resin was carried out with (5 × 3 mL) sodium diethyldithiocarbamate (0.5% solution in DMF) and subsequently with DCM (5 mL × 3) to produce **7**.

Fmoc-Phe-OH (2.3 g, 6.2 mmol) was added to **7** which was activated by HOBT (0.4 g, 3.1 mmol) and HBTU (0.99 g, 3.1 mmol) in DMF with the presence of DIPEA (6 mL, 37 mmol). The reaction mixture was stirred overnight (20 h) and washed with DMF (3 × 10 mL) and DCM (3 × 10 mL) respectively to yield **8**. Fmoc deprotection was performed using 20% piperidine in DMF, yielding compound 9. Fmoc-6-Ahx-OH (2.1 g, 6.2 mmol) was dissolved in DMF, and DIPEA (6 mL, 37 mmol), HOBT (0.4 g, 3.1 mmol), and HBTU (0.99 g, 3.1 mmol) were added. After stirring for 30 min compound **9** was added and reacted overnight to produce **10**. The Fmoc group was removed to yield compound **11**. The conjugation of HYNIC-BOC to compound **12** was performed by the addition of DIPEA, HOBT (0.4 g, 3.1 mmol), TBTU (0.99 g, 3.1 mmol) and reacted overnight. After the completion of the reaction the resin was cleaved by adding TFA : DCM (1 : 1) and stirred for 3 h then filtered to obtain compound **13** (PSMA-P1) in 42% overall yield. The crude obtained was purified by semi prep RP-HPL and confirmed by LC-MS (Fig. S5) and ^{1}H NMR (500 MHz, DMSO) δ 7.98–7.93 (d, J = 21 Hz, 1H), 7.7–7.69 (d, J = 10 Hz, 1H),7.24–7.21 (t, J = 7 Hz, 3H), 7.18–7.16 (d, J = 8.5 Hz, 3H), 6.86–6.85 (d, J = 7.5 Hz, 1H), 6.33–6.27 (d,d, J = 7 Hz, 1H), 4.02–4.14 (q, J = 17 Hz, 2H), 2.96–2.94 (q, J = 8 Hz, 8H), 2.27–2.04 (q, J = 10 Hz, 2H) (Fig. S6), ^{13}C-NMR (125 MHz, DMSO, δ = ppm) 176.74, 175.47, 174.72, 173.60, 167.86, 158.44, 157.32, 150.15, 140.34, 137.68, 129.38, 129.05, 127.15, 123.31, 113.43, 107.48, 86.21, 55.05, 53.82, 52.76, 30.47, 26.90, 24.26, 22.24, 19.83 (Fig. S7).

2.3 Kit formulation

A series of wet ^{99m}Tc-labeling of PSMA-P1 was conducted to optimize the quantities and concentrations of reagents, as well as the optimized temperature and labeling time served as the basis for developing the dry kit formulation. In the pre-formulation study for the kit, EDDA, tricine, and D-mannitol were subjected to optimized freeze-drying conditions for 24 h in a freeze dryer. This involved freezing the vial at −40 °C for 6 hours, followed by primary drying for 12 h and secondary drying at 0 °C for 2 hours and 20 °C for 4 h, after which the product was sealed under vacuum. The final kit formulation contains EDDA (10 mg), tricine (20 mg), D-mannitol (50 mg), stannous chloride dihydrate (50 μg), and PSMA-P1 (20 μg) in PBS buffer at pH 7.

2.4 Radiolabeling and quality control

Na[^{99m}TcO$_4^-$] (370–555 MBq, 1 mL) was added to the PSMA-P1 kit, and the vial was vortexed for 1 min to ensure mixing. The vial was placed in a boiling water bath at 100 °C for 20 minutes, then allowed to cool to room temperature. The radiochemical purity was assessed using ITLC-SG and radio-HPLC. The radio-HPLC analysis was employed the mobile phase consisting of 0.1% TFA in water (A) and 0.1% TFA in acetonitrile (B), with a gradient from 0% to 100% B over 30 minutes at a flow rate of 1 mL min^{-1}. Radio-TLC was performed according to the reported method.[38] The proposed structure of the complex is given in Scheme 1.

2.5 *In vitro* stability

The *in vitro* stability of the [^{99m}Tc]Tc-PSMA-P1 was evaluated in saline and human serum. [^{99m}Tc]Tc-PSMA-P1 (37 MBq, 100 μL) was added to saline (500 μL) and human serum (500 μL) separately, and stability was monitored over a period of 4 h. Aliquots of 100 μL were collected at 1, 2, 3, and 4 hours and mixed with an equal volume (100 μL) of ethanol and then centrifuged at 3000 rpm for 5 min. The resulting supernatant was analyzed, and quality control was performed as described in Section 2.4.

2.6 Determination of distribution coefficient

The distribution coefficient (log D) of [^{99m}Tc]Tc-PSMA-P1 was determined by the shake-flask method. In brief, [^{99m}Tc]Tc-PSMA-P1 was dissolved in PBS buffer (2 mL, 0.2 M, pH 7.4) to a concentration of 55.5 MBq mL^{-1}. An equal volume of anhydrous octanol (2 mL) was added and vortexed the mixture for 5 min, followed by centrifugation at 5000 rpm for 10 min. Aliquots (100 μL) from both the organic and aqueous phases were collected and measured using a γ-counter. The log D was calculated using the following formula:[39]

$$\text{Log } D = \log[(\text{counts in octanol phase})/(\text{counts in buffer phase})]$$

2.7 Cell uptake and *in vitro* binding affinity

The cellular uptake assay was carried out in 22Rv1 cells. Approximately 2 × 10^5 cells were plated in 24-well plates and allowed to incubate for 24 hours. After incubation, the wells were washed once with HBSS buffer (2 mL) to remove non-adherent cells. The cell was incubated with [^{99m}Tc]Tc-PSMA-P1 (0.3 μCi per well) for 4 h at 37 °C. Specific uptake was determined by blocking the cells with 100 μM of 2-(phosphonomethyl)-pentanedioic acid (2-PMPA). Following the incubation, the wells were washed twice with HBSS buffer (3 mL) to remove unbound radiotracer. Finally, the cells in each well were lysed using 0.5 mL of 0.5% SDS solution to analyze the bound radiotracer.

To determine the binding affinity (K_d), a saturation binding assay was carried out of [^{99m}Tc]Tc-PSMA-P1. The 22Rv1 cells (1 × 105 cells per well, 1 mL) were plated into a 24-well flat-bottom plate and allowed to form adherent for 24 h before the binding

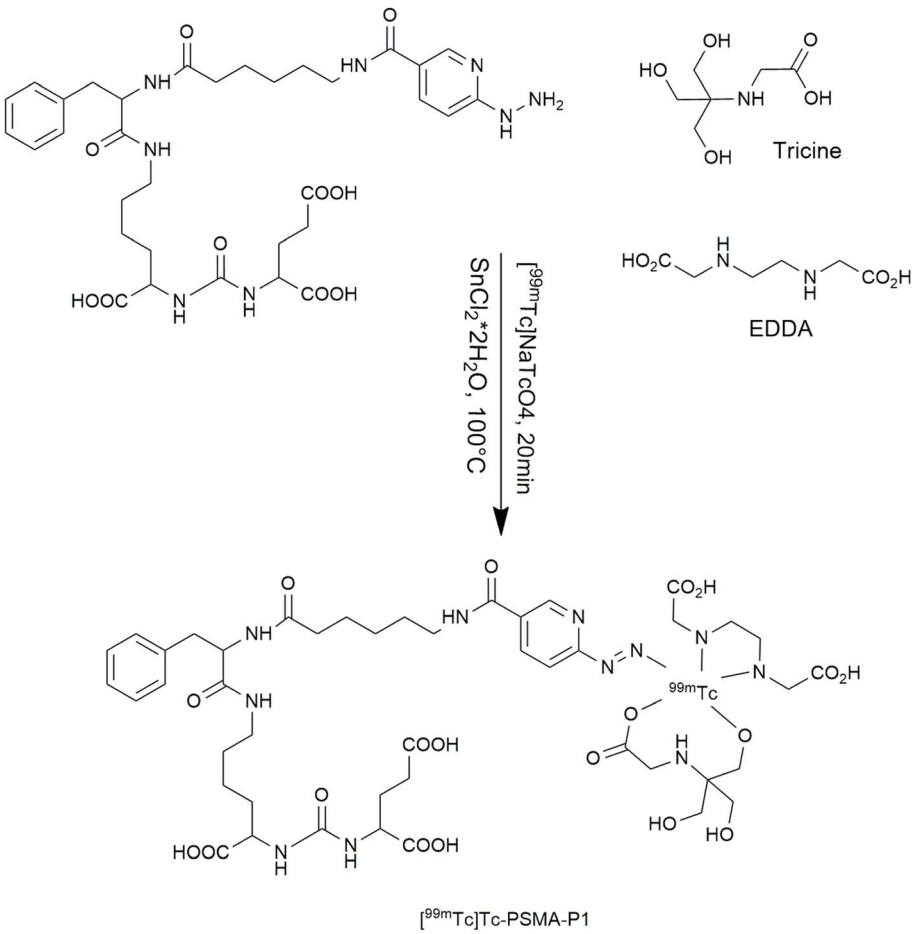

Scheme 1 Proposed structure of [^{99m}Tc]Tc-PSMA-P1.

experiment. The medium in each well was then replaced with HBSS supplemented with 1% BSA, containing serial dilution of [^{99m}Tc]Tc-PSMA-P1 in increasing concentration. Cells were incubated with the [^{99m}Tc]Tc-PSMA-P1 at 37 °C for 1 hour. After incubation, the medium was removed, and the cells were washed twice with 3 mL of HBSS to eliminate unbound radioactivity. The cells were then lysated by adding sodium dodecyl sulfate in PBS (0.5%, 500 μL) to each well and gently mixed before transferring to plastic tubes. The radioactivity of each sample was counted by γ-counter (PerkinElmer Wizard^2 automatic γ-counter), alongside reference samples representing the total amount of radioactivity initially added. Non-specific binding was assessed by co-incubating cells with 250 μM 2-PMPA, while specific binding was obtained by subtracting non-specific from total binding. The dissociation constant (K_d) was determined using a one-site binding model *via* non-linear regression analysis in GraphPad Prism 8 (GraphPad Software Inc., San Diego, CA, USA). All animal experiments were approved by the Institutional Animal Care and Use Committee (IACUC) of Seoul National University Hospital. The institution is accredited by the Association for Assessment and Accreditation of Laboratory Animal Care (AAALAC International), and all procedures were conducted by relevant guidelines and regulations.

2.8 *In vivo* biodistribution

All animal experiments were performed in compliance with the Seoul National University Hospital, Seoul, Korea, which is accredited by the Association for Assessment and Accreditation of Laboratory Animal Care (AAALAC International, 2007). The *in vivo* biodistribution of [^{99m}Tc]Tc-PSMA-P1 has been evaluated in male nude mice with 22Rv1 tumors. [^{99m}Tc]Tc-PSMA-P1 was injected into each mouse using a lateral tail vein. The mice expired at 4 h post-injection. The necessary organs and tissues were removed and preserved. To ensure the specific absorption, mice received a co-injection of 100 μg of 2-PMPA. The mean standard deviation is used to express values (SD).

2.9 SPECT/CT imaging

SPECT/CT imaging was performed 4 hours after intravenous administration of [^{99m}Tc]Tc-PSMA-P1 (11 MBq/200 μL) *via* the tail vein in BALB/c male nude mice bearing 22Rv1 tumors. To determine whether tumor uptake was PSMA-dependent, mice were co-injected with 100 μg of the potent inhibitor 2-PMPA. The mice were anesthetized with isoflurane and imaging was conducted using the NanoSPECT/CT system. The SPECT scanning parameters include γ-ray energy of 140 keV ± 10%, a matrix size of 256 × 256, five projections per angular step of 18°, and data acquisition using an ordered subset expectation

maximization algorithm with nine iterations. CT imaging was conducted using a tube voltage of 45 kV and an exposure time of 1.5 seconds per projection, with images reconstructed *via* cone-beam filtered back-projection. A Gaussian reconstruction filter was applied to the SPECT/CT images, and intensity scaling was adjusted to enhance visualization of the target organs.

2.10 First-in-human experience

All experiments were performed in accordance with the guidelines of Karachi Institute of Radiotherapy and Nuclear Medicine, Karachi (KIRAN, Karachi) and experiments were approved by ethical committee at KIRAN, Karachi. Informed consent was obtained from human participant of this study. One patient was successfully administered an intravenous injection of [^{99m}Tc]Tc-PSMA-P1 (370 MBq). Whole-body planar imaging was performed, followed by targeted SPECT-CT imaging of the pelvic region 2 hours post-injection. The acquisition parameters for SPECT were set at 10 min, with a peak energy of 140 keV, 10 seconds per projection, a matrix size of 128 × 128, and a zoom factor of 1. For CT, the parameters included an acquisition time of 2–3 minutes, a matrix size of 512 × 512, a DFOV of 50, 120 kV, 160 mA, and a slice thickness of 3.75 mm.

3 Results

3.1 Molecular docking

Docking simulation predicted that both labeled and non-labeled ligands have interactions within the active pockets of target receptors (PDB ID's: 2OOT, 2XW1, 2ZCH and 2XV7) related to prostate cancer or involve in its development. PSMA-P1 interactions and docking inside the active pocket of receptor protein PDB ID: 2OOT represented in ribbon form, a human glutamate carboxypeptidase II (GCPII) established marker for prostate-cancer see Fig. 1 while remaining PSMA-P1 and [^{99m}Tc]Tc-PSMA-P1 docking with receptor proteins (PDB ID's: 2OOT, 2XW1, 2ZCH and 2XV7) and their adjustment inside the active pockets magnified form is represented in Fig. S3 and S4. Which is further elaborated in 2D diagrams to represent ligand and protein bonding and nonbonding interactions. Fig. 2 (A) shows that PSMA-P1 interacted with receptor protein PDB-ID 2OOT *via* hydrogen bonding with residues *i.e.* GLY 548, TYR 234, ASN 698, LYS 207. Similarly Fig. S6 represents PSMA-P1 interactions with receptor PDB ID's: 2XW1, 2ZCH and 2XV7. Whereas Fig. 2 (B) predicts the [^{99m}Tc]Tc-PSMA-P1 interactions with PDB ID: 2OOT *via* PRO237, VAL239, GLY238, PHE235, TRP246, LYS240, PHE565. 2D diagram of [^{99m}Tc]Tc-PSMA-P1 interactions with receptor PDB ID's: 2XW1, 2ZCH and 2XV7 prepresented in Fig. S7. Docking simulation procedure validated through reference compounds HYNIC-ALUG and [^{99m}Tc]Tc-HYNIC-ALUG and docked with PDB ID: 2OOT receptor is shown in Fig. S5. Furthermore, the experimental log P (-2.55 ± 0.130) is close to the calculated values (clog P -4.177 and clog S -1.007), supporting the validity of *in silico* studies. Toxicity risk calculations also predicted no mutagenic, irritating, or reproductive toxicities (Tables S3 and S4). PSMA quantitative structure–activity relationship (QSAR) calculations were performed for the PSMA-P1 ligand and [^{99m}Tc]Tc-PSMA-P1 complex. The HOMO–LUMO energy gap was found 0.17292 eV for the PSMA-P1 ligand and 0.01085 eV for [^{99m}Tc]Tc-PSMA-P1 indicating more reactivity of the complex as compared to the non-labeled molecule, as shown in Fig. 3.

3.2 Chemistry

Compound **2** was synthesized by reacting 2-CTCresin with Fmoc-Lys(Alloc)-OH (**1**) followed by removal of Fmoc group generated **3**. The core PSMA-binding motif (compound **6**) was synthesized by reacting compound **4** (*t*-Bu-Glu·HCl) with triphosgene and DIPEA at 0 °C to form intermediate isocyanate **5**, which was then coupled with 2-CTC-Lys (Alloc) to yield compound **6**. The allyloxycarbonyl (alloc) protecting group was

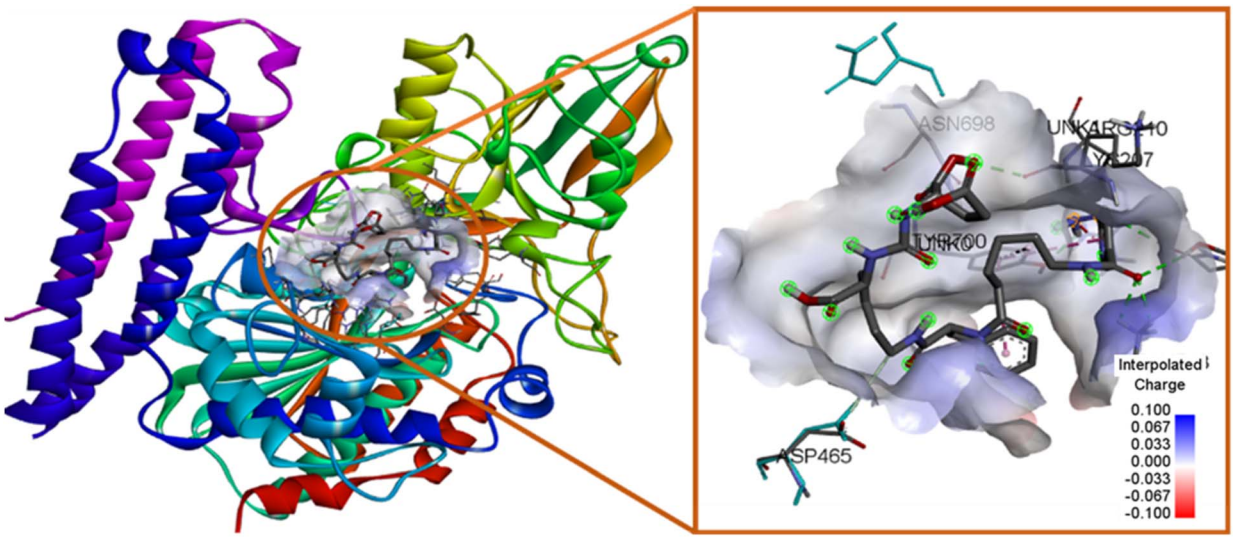

Fig. 1 PSMA-P1 interactions with receptor PDB ID 2OOT represented in ribbon form and magnified inside the active site with electrostatic potential on molecule surface.

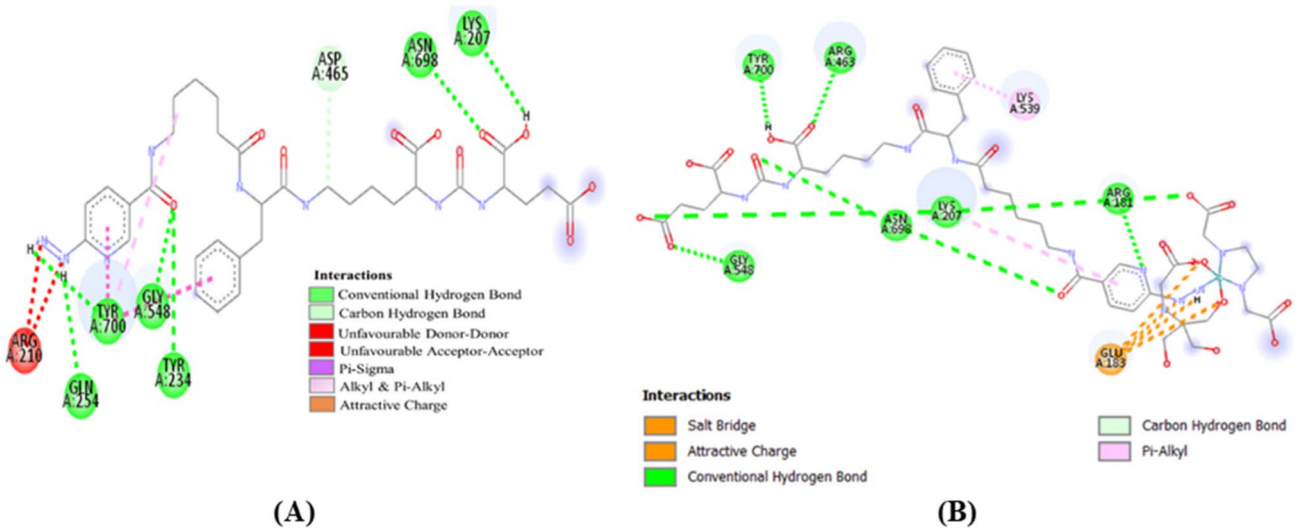

Fig. 2 PSMA-P1 and [^{99m}Tc]Tc-PSMA-P1 interaction types with receptor PDB ID 2OOT residues represented in 2D diagram (A) and (B) respectively.

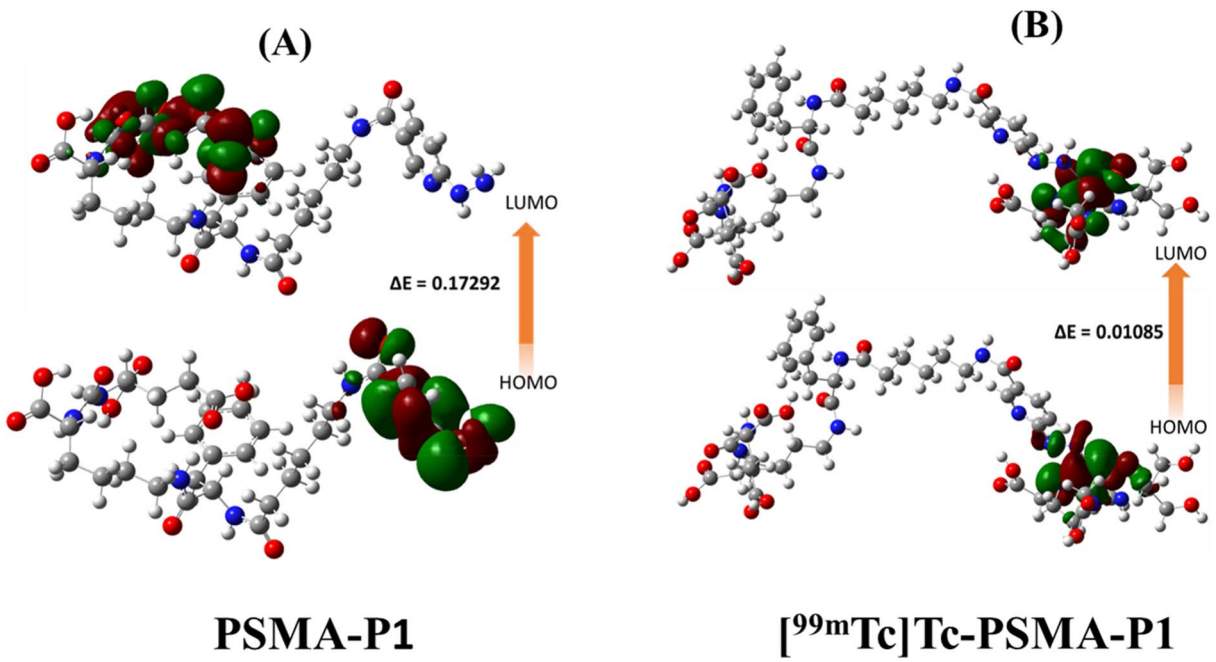

Fig. 3 HUMO–LUMO energy gap of both PSMA-P1 (A) and [^{99m}Tc]Tc-PSMA-P1 (B).

removed by $Pd[P(C_6H_5)_3]_4$ catalyst to give **7** and followed by the reaction with Fmoc-Phe-OH using coupling reagents such as TBTU & HOBT to obtain **8**. The Fmoc group was selectively deprotected from **8** using 20% piperidine/DMF and produced **9**. Similarly, Fmoc-6-Ahx-OH conjugated to compound **9**, followed by removing the Fmoc group generated **11** by following the same protocol described above. To obtain compound **12**, compound **11** was reacted with HYNIC-Boc in the presence of the coupling agents HOBT and TBTU. Subsequently, 2-CTC resin, and other bulky functional groups (Boc and *t*-Bu) were simultaneously removed by 1 : 1 (v/v) mixture of TFA and DCM was employed for the synthesis of compound **13**. PSMA-P1 (Scheme S1). The final compound **12** was purified by prep-HPLC (Fig. 4) and confirmed by LC-MS (Fig. S8), and ^{1}H-NMR, ^{13}C-NMR (Fig. S9 and S10).

3.3 Radiolabeling of freeze-dried kit

[^{99m}Tc]Tc-PSMA-P1 was prepared using a straightforward one-step kit-based labeling method. Radiochemical purity was evaluated using both radio-TLC and radio-HPLC techniques. Analysis by radio-thin layer chromatography (radio-TLC) involved two systems to effectively differentiate [^{99m}Tc]Tc-

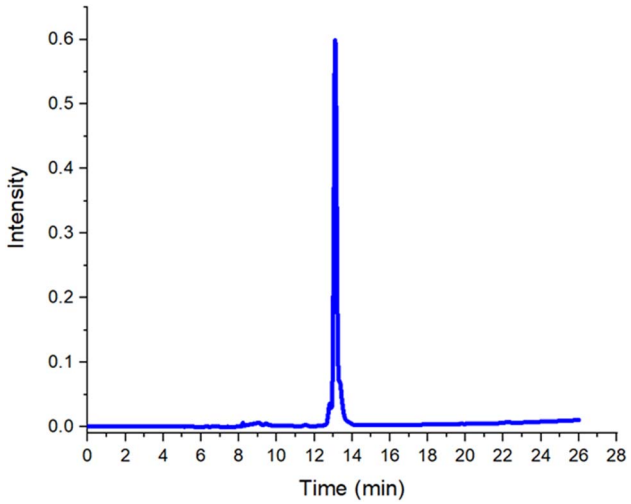

Fig. 4 Analytical HPLC chromatogram of PSMA-P1.

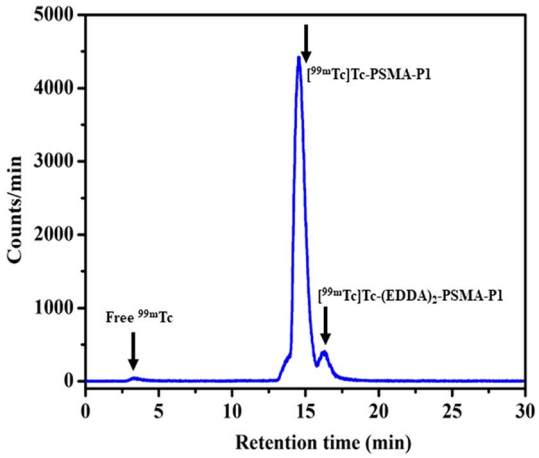

Fig. 6 Radio-HPLC of [^{99m}Tc]Tc-PSMA-P1 in CAN/water in gradient.

PSMA-P1 complex from impurities including [^{99m}Tc]$NaTcO_4$ (Free ^{99m}Tc) and [^{99m}Tc]$TcO_2 \cdot nH_2O$ (Colloid). The radio-TLC chromatogram for the labeled complex and these impurities in both systems is shown in Fig. 5. In acetone, [^{99m}Tc]Tc-PSMA-P1 complex stayed at baseline (R_f = 0.1–0.2) and the solvent carried free ^{99m}Tc toward the front (R_f = 0.9–0.1) (Fig. 5A). Using ACN : H_2O (1 : 1) as the developing solvent, [^{99m}Tc]Tc-PSMA-P1 migrated with the solvent front (R_f = 0.9–1.0) and free Na [^{99m}TcO_4] remained at the origin (R_f = 0–0.1) (Fig. 5B). Moreover, radio-HPLC analysis showed a retention time of 14.5 minutes from the [^{99m}Tc]Tc-PSMA-P1 (Fig. 6). Both radio-TLC and radio-HPLC confirmed a radiochemical purity ≥99%. Furthermore, the proposed structure of [^{99m}Tc]Tc-PSMA-P1, illustrating the coordination of the ligand with ^{99m}Tc is depicted in Scheme 1.

3.4 Stability study and determination of partition coefficient

The *in vitro* stability of [^{99m}Tc]Tc-PSMA-P1 was evaluated in both saline and human serum at 37 °C and demonstrated high stability for up to 4 hours (Fig. 7). This result indicates that ≥95% of [^{99m}Tc]Tc-PSMA-P1 remains intact and stable under physiological conditions, which is crucial for its potential use in diagnostic imaging. Additionally, to assess its lipophilicity, the partition coefficient (log *D*) of [^{99m}Tc]Tc-PSMA-P1 involved partitioning the compound between octanol and phosphate-buffered saline (PBS, pH 7.4). The log *D* value obtained was −2.55 ± 0.130, indicating its hydrophilic nature, which may support its biodistribution in targeting tissues with minimal off-target uptake. These characteristics underscore the promise of [^{99m}Tc]Tc-PSMA-P1 for *in vivo* imaging applications.

3.5 Cell uptake and *in vitro* binding affinity (K_d)

The cell uptake results for [^{99m}Tc]Tc-PSMA-P1 in the 22Rv1 cell line, presented in Fig. 8A, indicate a marked difference between the non-blockade and blockade conditions. In the non-blockade condition, [^{99m}Tc]Tc-PSMA-P1 exhibited a high uptake of 22%. However, when cells were pre-treated with 2-PMPA to block PSMA receptors, uptake significantly decreased to 5%, representing a substantial 77% reduction. Saturation binding assays with

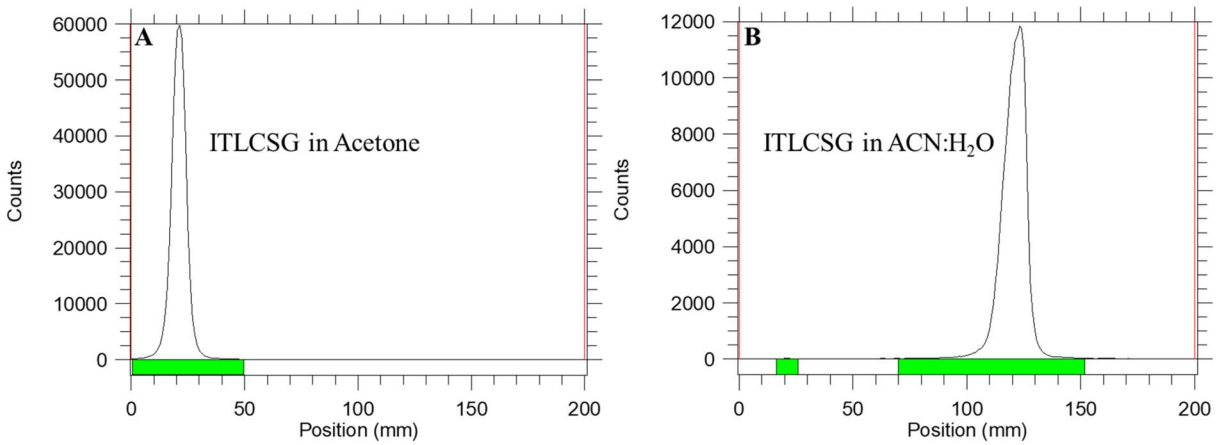

Fig. 5 Radio-ITLC-SG chromatogram showing RCY of [^{99m}Tc]Tc-PSMA-P1 developed in acetone solvent (A), ITLC-SG chromatogram showing RCY of [^{99m}Tc]Tc-PSMA-P1 in ACN:H_2O solvent system (B).

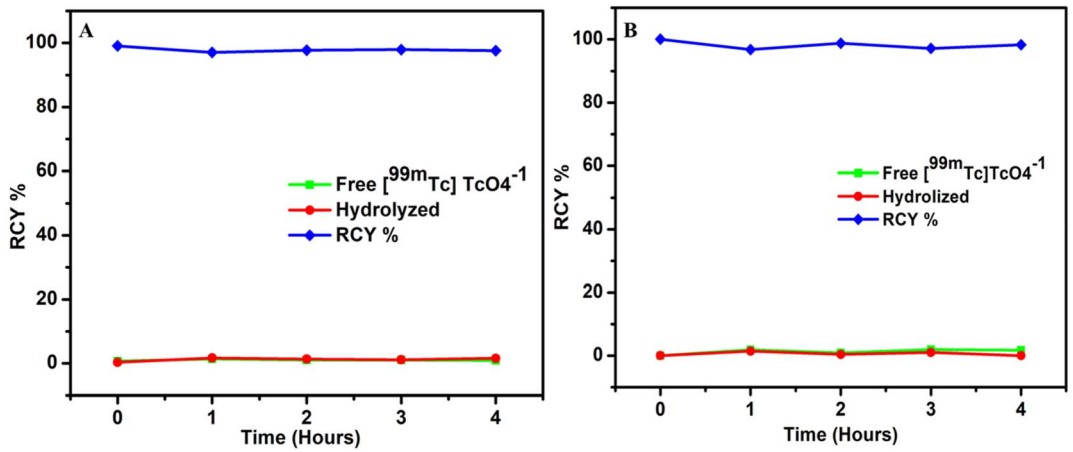

Fig. 7 Stability of [^{99m}Tc]Tc-PSMA-P1 determined by radio-TLC (A) saline (B) human serum.

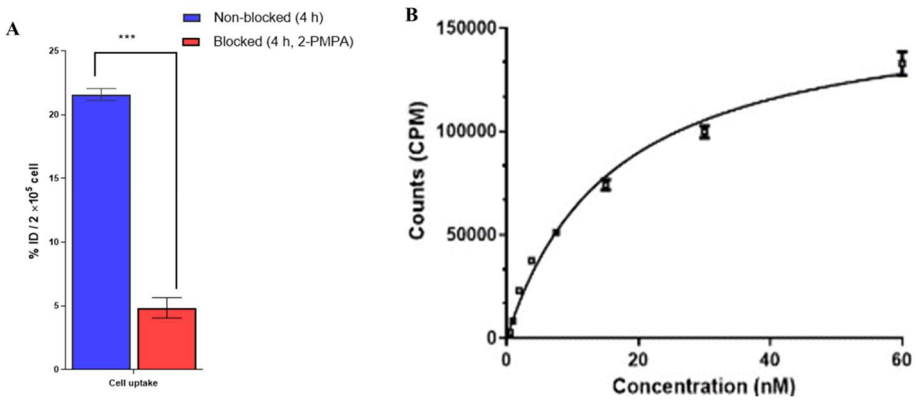

Fig. 8 (A) cell uptake study in 22Rv1 cell line at 4 h (B) saturation binding curve of [^{99m}Tc]Tc-PSMA-P1 for the determination of K_d value.

22RV1 cells were conducted to evaluate the binding affinity of [^{99m}Tc]Tc-PSMA-P1. [^{99m}Tc]Tc-PSMA-P1 exhibited strong binding to 22Rv1 cells confirming high affinity for PSMA. The saturation binding curve is shown in Fig. 8B. The estimated dissociation constant (K_d) was calculated using nonlinear regression (16.14 ± 1.452 nM) highlights the effectiveness of [^{99m}Tc]Tc-PSMA-P1 for targeted imaging in prostate cancer diagnostics.

3.6 Biodistribution

In 22Rv1 tumor-bearing BALB/c male mice, [^{99m}Tc]Tc-PSMA-P1 was administered at 1 and 4 hours post-tail vein injection (Table 1).[^{99m}Tc]Tc-PSMA-P1 demonstrated tumor uptake of (1.91 ± 0.91% ID g^{-1}) at 1 hour and (1.68 ± 0.16% ID g^{-1}) ($P \leq 0.001$) decreased at 4 h post injection. As predicted, the kidney showed a low concentration of [^{99m}Tc]Tc-PSMA-P1 conjugate at 1 h and further decreased at 4 h post-injection as compared to [^{99m}Tc]Tc-HYNIC-ALUG. After co-injection of 2-PMPA, the kidney uptake was prominently reduced to (5.70 ± 0.67% ID g^{-1}) at 1 hour and (3.86 ± 0.65% ID g^{-1}) at 4 hours after injection, respectively. However, the study is limited by the small sample size and the use of a single tumor model. Additionally, inter-animal variability in tracer uptake introduces some imprecision in the quantification of biodistribution results.

3.7 SPECT/CT imaging

To assess the *in vivo* PSMA-targeting potential of [^{99m}Tc]Tc-PSMA-P1 imaging, whole-body SPECT/CT scans were conducted at 4 hours post-injection in BALB/c male nude mice bearing 22Rv1 tumors.[^{99m}Tc]Tc-PSMA-P1 exhibited enhanced tumor-to-background contrast and was eliminated *via* the kidneys (Fig. 9A). Tumor uptake was entirely inhibited when co-injected with 2-PMPA (Fig. 9B).

3.8 First-in-human study

A preliminary clinical evaluation of [^{99m}Tc]Tc-PSMA-P1 was performed in a patient with metastatic prostate cancer (PCa). SPECT/CT imaging is shown in Fig. 10 following an injection of 370 MBq of [^{99m}Tc]Tc-PSMA-P1. The images demonstrated physiological tracer uptake in various organs, consistent with expected biodistribution. Notably, there was distinct uptake observed in the D9 vertebra and the left median lobe of the prostate, indicating areas of PSMA expression. The imaging also highlighted [^{99m}Tc]Tc-PSMA-P1 sensitivity in identifying lymph node metastases, underscoring its potential as a promising PSMA-targeted SPECT radiotracer for detecting metastatic PCa. This initial result supports the compound's further exploration

Table 1 Biodistribution of [^{99m}Tc]Tc-PSMA-P1 in PSMA-expressing 22Rv1 tumor-bearing BALB/c male nude mice at 1 and 4 h post-injection[a]

Percentage of injected dose per gram (% ID g^{-1})				
Organ	1 hour	4 hours	1 hour blocked	4 hours blocked
Blood	0.48 ± 0.05	0.19 ± 0.02	0.78 ± 0.13	0.22 ± 0.03
Heart	0.41 ± 0.04	0.18 ± 0.03	0.45 ± 0.07	0.11 ± 0.01
Lung	0.54 ± 0.03	0.35 ± 0.04	0.86 ± 0.05	0.45 ± 0.04
Liver	1.21 ± 0.21	0.69 ± 0.11	1.54 ± 0.28	1.22 ± 0.16
Spleen	0.43 ± 0.24	1.68 ± 0.77	0.37 ± 0.04	0.19 ± 0.05
Stomach	0.69 ± 0.15	0.37 ± 0.08	0.75 ± 0.26	0.22 ± 0.04
Intestine	0.49 ± 0.14	1.39 ± 0.04	0.85 ± 0.07	1.28 ± 0.15
Kidney	51.02 ± 3.48***	36.73 ± 2.96***	5.70 ± 0.67	3.86 ± 0.65
Muscle	0.17 ± 0.08	0.10 ± 0.04	0.20 ± 0.07	0.05 ± 0.01
Bone	0.61 ± 0.17	0.40 ± 0.10	0.44 ± 0.12	0.42 ± 0.15
Tail	0.44 ± 0.04	0.44 ± 0.07	0.88 ± 0.28	0.52 ± 0.07
Tumor	1.91 ± 0.19***	1.68 ± 0.16***	0.36 ± 0.09	0.34 ± 0.07

[a] Data are presented as % ID g^{-1} (mean ± SD; $n = 4$). Blocking studies were conducted by co-injecting 100 μg of 2-PMPA. Statistical significance was denoted as *$p \leq 0.001$; *** high uptake.

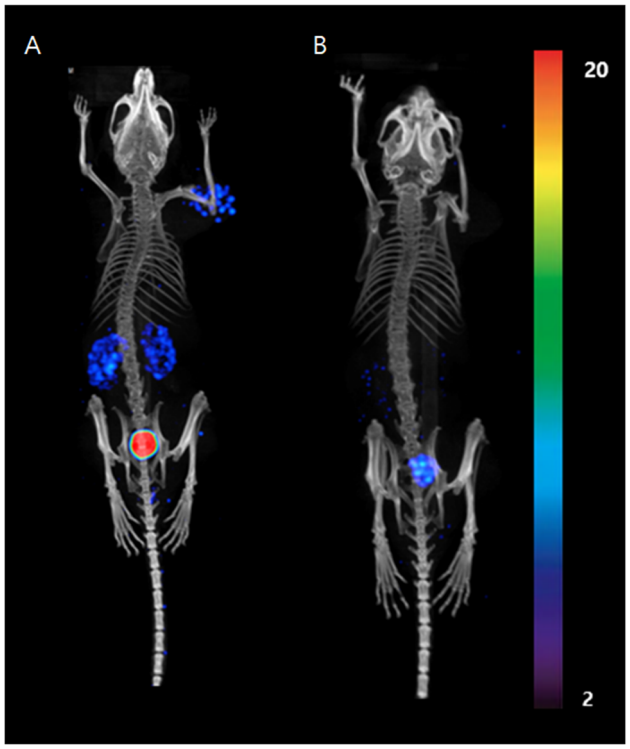

Fig. 9 Whole-body SPECT/CT imaging of [^{99m}Tc]Tc-PSMA-P1 in 22Rv1 tumor-bearing mice targeting PSMA at 4 hours post-injection. [^{99m}Tc]Tc-PSMA-P1 alone. (A) Blockade by co-injection of 2-PMPA (100 μg) (B).

for broader clinical use in PCa imaging, providing a specific and effective tool for detecting PSMA-positive lesions.

4 Discussion

Specific and strong interaction of the Glu-Urea-Lys motif with PSMA has been confirmed through PET/CT imaging techniques. The recent development of cadmium–zinc–telluride (CZT) semiconductor detectors has improved the image quality of SPECT/CT, enhancing resolution and reducing scanning time. Given widespread availability, cost-effectiveness, and favorable physical properties, ^{99m}Tc is well-suited for SPECT/CT,[40] particularly in setting where PET/CT is not available providing an effective alternative for diagnosis of cancer.

Urea-based ^{99m}Tc-labeled PSMA inhibitors have been developed by using variety of different linkers and chelator to tumor targeting potential for PCa imaging. Hydrazinonicotinic acid (HYNIC) has emerged as a valuable bifunctional chelator for ^{99m}Tc due to its capacity to bind in one or two coordination sites, making it necessary to add coligand ethylenediamine-*N*,*N*′-diacetic acid (EDDA) and tricine to stabilize the ^{99m}Tc-core. This approach enhances radiochemical yield and stability, inspiring further research into HYNIC-labeled PSMA agents, such as [^{99m}Tc]Tc-EDDA/HYNIC-iPSMA,[41], [^{99m}Tc]-PSMA-T4,[22] which have shown improved imaging and better pharmacokinetics.

Molecular docking simulations were performed to predict the pharmacokinetic and toxicological properties of newly designed PSMA-P1 (Tables S3 and S4). The ligand PSMA-P1 and radiolabeled complex [^{99m}Tc]Tc-PSMA-P1 were analyzed to check the interaction with prostate-specific receptors models (PDB code: 2ZCH, 2XW1, 2XV7, and 2OOT), revealing binding affinities of −0.55, 0.85, −2.79, −4.98 kcal mol^{-1}, respectively (Table S1). The PSMA receptor model 2OOT showed the strongest binding affinity with [^{99m}Tc]Tc-PSMA-P1, having a docking score of −4.98 kcal mol^{-1} and an inhibition constant (K_i) of 69.14 μM, and comparable to previous,[24] demonstrating a slightly higher binding affinity for [^{99m}Tc]Tc-HYNIC-PSMA-P1 (−4.98 kcal mol^{-1}) *versus* the non-labeled peptide, PSMA-P1 (−4.46 kcal mol^{-1}), indicating successful binding and structural suitability. [^{99m}Tc]Tc-HYNIC-ALUG was also simulated with the 2OOT model (Fig. S4), facilitating direct comparison. PSMA-P1 showed a binding affinity of −2.79 kcal mol^{-1} with a K_i of 222.81 μM (Table S1), which was slightly higher than HYNIC-ALUG binding energy of −2.19 kcal mol^{-1} and K_i of 253 μM

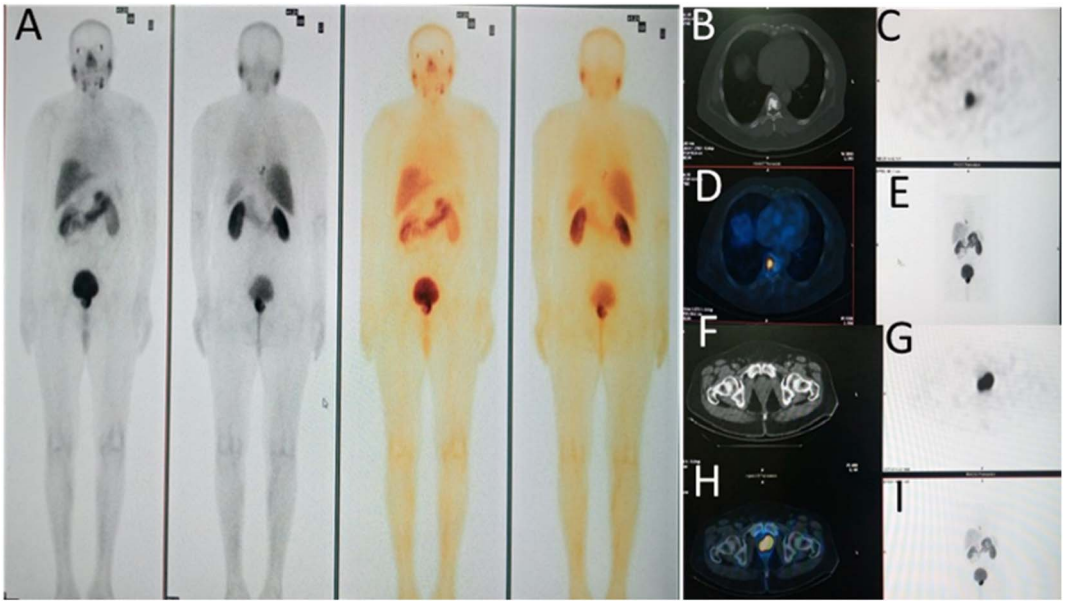

Fig. 10 A prostate cancer patient Physiological bio-distribution of [^{99m}Tc]Tc-PSMA-P1 (A) whole body scan. (B–E) SPECT/CT images showing marked expression o [^{99m}Tc]Tc-PSMA-P1 in D9 vertebra; consistent with metastasis, (F and G)SPECT/CT images showing marked expression of [^{99m}Tc]Tc-PSMA-P1 in both lobes of prostate glands, (H and I) SPECT-CT images reveal PSMA avid area involving left median lobe of the prostate gland.

(Table S2). Notably, the K_i of [^{99m}Tc]Tc-PSMA-P1 was found to be lower (69.14 μM) than that of [^{99m}Tc]Tc-HYNIC-ALUG (80.2 μM), suggesting a tighter binding. The enhanced binding energy of the labeled peptide [^{99m}Tc]Tc-PSMA-P1 (−4.98 kcal mol^{-1}) relative to the unlabeled PSMA-P1 (−4.46 kcal mol^{-1}) further supports the docking's effectiveness. In the QSAR analysis, the HOMO–LUMO energy gap (0.01085 eV) and dipole moment (7.0141 debye) demonstrated significant bioreactivity and polarizability for the [^{99m}Tc]Tc-PSMA-P1. The Molecular Electrostatic Potential (MESP) analysis, illustrated in Fig. 1, identified a highly electrophilic zone (highlighted in red) around the ^{99m}Tc-labeled region Fig. 2, suggesting enhanced reactivity compared to the non-labeled section in Fig. 1, making it well-suited for forming hydrogen bonds with amino acid residues.

The PSMA-P1 was synthesized *via* the SPPS, achieving high chemical purity (≥99%) following purification through semi-preparative HPLC. For radiolabeling, HYNIC-PSMA-P1 was successfully labeled with ^{99m}Tc, resulting in a high radiochemical purity (≥99%), verified by both radio-TLC (Fig. 5) and radio-HPLC (Fig. 6). [^{99m}Tc]Tc-PSMA-P1 exhibited high stability in saline and human serum for up to 4 h maintaining radiochemical purity ≥95% without degradation (Fig. 7). The log *D* value of [^{99m}Tc]Tc-PSMA-P1 is −2.55 ± 0.130 slightly less than [^{99m}Tc]Tc-HYNIC-ALUG (−2.68 ± 0.12). The addition of the aromatic group has marginally increased the lipophilicity of [^{99m}Tc]Tc-HYNIC-PSMA-P1. Overall, [^{99m}Tc]Tc-PSMA-P1 remains hydrophilic, as log *D* value ≤2.00 which supports its renal excretion pathway.[1]

The cell uptake results of [^{99m}Tc]Tc-PSMA-P1 in the 22Rv1 cell line shown in Fig. 8A, reveal a significant difference between the non-blockade and blockade. The substantial reduction under the blockade condition demonstrates that [^{99m}Tc]Tc-HYNIC-PSMA-P1 binding to cells is mediated by PSMA, confirming the high selectivity for PSMA-expressing cells. Further, the high affinity of [^{99m}Tc]Tc-PSMA-P1 for PSMA was confirmed with low dissociation constant value (K_d) (16.14 ± 1.45 nM) determined by saturation binding assay (Fig. 8B). In 22Rv1 tumor-bearing BALB/c nude mice, the tissue distribution of [^{99m}Tc]Tc-PSMA-P1 was assessed at 1 and 4 h after tail vein injection (Table 1). [^{99m}Tc]Tc-PSMA-P1 demonstrated immediate accumulation in tumor tissue at 1 h and showed retention even at 4 h post-injection. The uptake was dramatically decreased with co-injection of 2-PMPA, indicating that [^{99m}Tc]Tc-PSMA-P1 uptake is PSMA mediated. Moreover, the biodistribution results reveal a clear shift in excretion patterns between [^{99m}Tc]Tc-PSMA-P1 and [^{99m}Tc]Tc-PSMA I&S, particularly in the kidneys, liver, spleen and intestine. The significant reduction in kidney (51.02 ± 3.48 *vs.*186 ± 23), liver (1.21 ± 0.21 *vs.* 1.58 ± 0.24 *vs.*), spleen (0.43 ± 0.24 *vs.* 47 ± 17) and intestinal uptake (0.49 ± 0.14 *vs.* 2.46 ± 0.14) in [^{99m}Tc]Tc-PSMA-P1 suggests a decreased hepatobiliary clearance compared to [^{99m}Tc]Tc-PSMA I&S. This indicates that the phenyl modification in PSMA-P1 altered its elimination pathway, leading to a preferential renal clearance rather than biliary excretion. The lower hepatic and intestinal uptake suggests reduced interaction with liver transporters, minimizing hepatobiliary retention. This modification helps overcome the high retention in the kidney, and hepatobiliary excretion drawback associated with [^{99m}Tc]Tc-PSMA I&S.[17]

The SPECT/CT image (Fig. 10) illustrates the distribution of [^{99m}Tc]Tc-PSMA-P1 in a prostate cancer patient, with notable uptake detected in the kidneys, salivary and lacrimal glands,

intestines, and urinary bladder and PSMA expression in specific areas (Fig. 10A) which is concordance with the [^{99m}Tc]Tc-PSMA-4.[42] In Fig. 10B–E, SPECT/CT images reveal a marked accumulation of the radiotracer in the D9 vertebra, which is consistent with metastatic involvement. This localization supports the use of [^{99m}Tc]Tc-HYNIC-PSMA-P1 in detecting skeletal metastases, as PSMA is often overexpressed in metastatic lesions. Significant uptake in both lobes of the prostate gland, indicating elevated PSMA expression within the primary tumor site (Fig. 10F and G). This localized tracer accumulation in the prostate confirms its value in identifying areas with high PSMA expression. (Fig. 10H and I) Demonstrate a PSMA-avid area specifically within the left median lobe of the prostate, suggesting focal PSMA expression in this region. Overall, this distribution pattern supports the utility of [^{99m}Tc]Tc-PSMA-P1 for effectively targeting PSMA-expressing cells in primary tumor sites and potential metastatic locations, and further extended for evaluation in more patients.

Conclusion

The PSMA-P1 ligand was designed, successfully synthesized, and labeled with ^{99m}Tc to develop [^{99m}Tc]Tc-PSMA-P1. Molecular docking studies indicated that both PSMA-P1 and [^{99m}Tc]Tc-PSMA-P1 exhibited a strong binding affinity. The [^{99m}Tc]Tc-PSMA-P1 displayed excellent *in vitro* stability (≥95% for up to 4 h) and high PSMA-specific affinity. A stable, reproducible, lyophilized kit was developed for easy preparation for [^{99m}Tc]Tc-PSMA-P1. The biodistribution and small animal SPECT/CT showed high tumor uptake and retention. A first patient study demonstrated its effectiveness as a diagnostic agent for PSMA-expressing lesions, with further clinical evaluation needed to confirm its broader applicability.

Author contributions

Writing – original draft, data curation, investigation, validation, writing – review & editing, Maria Hassan; supervision, methodology, visualization, review & editing, data curation, Tanveer Hussain Bokhari; software, methodology, visualization, formal analysis, Faiz Ahmed; resources, conceptualization, funding acquisition, project administration, Yun-Sang Lee; supervision, conceptualization, project administration, methodology, resources, Nadeem Ahmed Lodhi.

Conflicts of interest

No potential conflicts of interest relevant to this article exist.

Data availability

The data supporting the findings of this study are available within the article [and/or] its SI.

The supplementary information contain the synthesis scheme of HYNIC-PSMA-P1, docking results and LC-MS and NMR data. See DOI: **https://doi.org/10.1039/d5ra04397b**.

Acknowledgements

This research was supported by the Ministry of Health and Welfare of Korea government (RS-2023-KH137294 and RS-2023-00263720). The Pakistan Institute of Nuclear Science and Technology (PINSTECH), Islamabad, Pakistan, supported the work, and all the authors would like to acknowledge Dr Rashid Nazir, Principal scientist, PINSTECH, for his constant support in providing HPLC.

References

1 K. Lu, C. Zhang, Z. Zhang, H.-T. Kuo, N. Colpo, F. Bénard and K.-S. Lin, *Molecules*, 2023, **28**, 5120.
2 A. Bernal, A. J. Bechler, K. Mohan, A. Rizzino and G. Mathew, *Pharmaceuticals*, 2024, **17**, 351.
3 C. Rojas, S. T. Frazier, J. Flanary and B. S. Slusher, *Anal. Biochem.*, 2002, **310**, 50–54.
4 F. Lundmark, G. Olanders, S. S. Rinne, A. Abouzayed, A. Orlova and U. Rosenström, *Pharmaceutics*, 2022, **14**, 1098.
5 M. I. Davis, M. J. Bennett, L. M. Thomas and P. J. Bjorkman, *Proc. Natl. Acad. Sci. U. S. A.*, 2005, **102**, 5981–5986.
6 Q. Hu, K. Padron, D. Hara, J. Shi, A. Pollack, R. Prabhakar and W. Tao, *ACS Omega*, 2021, **6**, 33354–33369.
7 M. El Fakiri, N. M. Geis, N. Ayada, M. Eder and A.-C. Eder, *Cancers*, 2021, **13**, 3967.
8 F. Kampmeier, J. D. Williams, J. Maher, G. E. Mullen and P. J. Blower, *EJNMMI Res.*, 2014, **4**, 1–10.
9 S. Debnath, N. Zhou, M. McLaughlin, S. Rice, A. K. Pillai, G. Hao and X. Sun, *Int. J. Mol. Sci.*, 2022, **23**, 1158.
10 U. Hennrich and M. Eder, *Pharmaceuticals*, 2021, **14**, 713.
11 A. F. Voter, R. A. Werner, K. J. Pienta, M. A. Gorin, M. G. Pomper, L. B. Solnes and S. P. Rowe, *Expert Rev. Anticancer Ther.*, 2022, **22**, 681–694.
12 M. J. Morris, S. P. Rowe, M. A. Gorin, L. Saperstein and F. Pouliot, *Clin. Cancer Res.*, 2021, **27**, 3674–3682.
13 S. Hasan and M. A. Prelas, *SN Appl. Sci.*, 2020, **2**, 1782.
14 N. A. Lodhi, J. Y. Park, M. K. Hong, Y. J. Kim, Y.-S. Lee, G. J. Cheon and J. M. Jeong, *Bioorg. Med. Chem.*, 2019, **27**, 1925–1931.
15 J. Nairne, P. B. Iveson and A. Meijer, *Prog. Med. Chem.*, 2015, **54**, 231–280.
16 A. Faheem, T. Bokhari, S. Roohi, A. Mushtaq and M. Sohaib, *Nucl. Med. Biol.*, 2013, **40**, 148–152.
17 S. Robu, M. Schottelius, M. Eiber, T. Maurer, J. Gschwend, M. Schwaiger and H.-J. Wester, *J. Nucl. Med.*, 2017, **58**, 235–242.
18 H. Rathke, A. Afshar-Oromieh, F. L. Giesel, C. Kremer, P. Flechsig, S. Haufe, W. Mier, T. Holland-Letz, M. De Bucourt and T. Armor, *J. Nucl. Med.*, 2018, **59**, 1373–1379.
19 S. Urbán, C. Meyer, M. Dahlbom, I. Farkas, G. Sipka, Z. Besenyi, J. Czernin, J. Calais and L. Pávics, *J. Nucl. Med.*, 2021, **62**, 1075–1081.
20 D. Papagiannopoulou, in *Handbook of Radiopharmaceuticals: Methodology and Applications*, ed. M. R. Kilbourn and P. J. H. Scott, Willey, 2020, pp. 375–433.

21 S. Hillier, K. Maresca, G. Lu, J. Marquis, C. Zimmerman, S. Nimmagadda, W. Eckelman, M. Pomper, J. Joyal and J. Babich, *J. Nucl. Med.*, 2010, **51**, 481.
22 M. Maurin, M. Wyczółkowska, A. Sawicka, A. E. Sikora, U. Karczmarczyk, B. Janota, M. Radzik, D. Kłudkiewicz, J. Pijarowska-Kruszyna and A. Jaroń, *Molecules*, 2022, **27**, 7216.
23 E. Mamlins, L. Scharbert, J. Cardinale, M. Krotov, E. Winter, H. Rathke, B. Strodel, A. O. Ankrah, M. Sathekge and U. Haberkorn, *Mol. Imaging Biol.*, 2024, **26**, 81–89.
24 T. H. Bokhari, F. Bibi, M. Irfan, F. Ahmed, T. A. Rahman, S. Fatima, M. Zeeshan, M. Hassan, A. S. Ullah and M. Wasim, *Iran. J. Nucl. Med.*, 2024, 140–149.
25 X. Xu, J. Zhang, S. Hu, S. He, X. Bao, G. Ma, J. Luo, J. Cheng and Y. Zhang, *Nucl. Med. Biol.*, 2017, **48**, 69–75.
26 C. Helgen and C. G. Bochet, *J. Org. Chem.*, 2003, **68**, 2483–2486.
27 M.-C. Chien, Y. K. Lin, Y. Liao, S.-H. Chen, Y.-W. Chen, C.-Y. Liang, V. Molakaseema, S. C. Hsu, C.-C. Lin and H.-T. Chen, *ACS Omega*, 2023, **8**, 41855–41864.
28 C. Barinka, J. Starkova, J. Konvalinka and J. Lubkowski, *Acta Crystallogr. Sect. F Struct. Biol. Cryst. Commun.*, 2007, **63**, 150–153.
29 R. Ménez, S. Michel, B. H. Muller, M. Bossus, F. Ducancel, C. Jolivet-Reynaud and E. A. Stura, *J. Mol. Biol.*, 2008, **376**, 1021–1033.
30 A. J. Ryan, J. Ghuman, P. A. Zunszain, C.-w. Chung and S. Curry, *J. Struct. Biol.*, 2011, **174**, 84–91.
31 V.-M. Leppänen, M. Jeltsch, A. Anisimov, D. Tvorogov, K. Aho, N. Kalkkinen, P. Toivanen, S. Ylä-Herttuala, K. Ballmer-Hofer and K. Alitalo, *Blood*, 2011, **117**, 1507–1515.
32 A. Grosdidier, V. Zoete and O. Michielin, *Nucleic Acids Res.*, 2011, **39**, W270–W277.
33 *BIOVIA Discovery Studio Visualizer,* Dassault Systèmes, 2021.
34 M. J. Frisch, G. W. Trucks, H. B. Schlegel, G. E. Scuseria, M. A. Robb, J. R. Cheeseman, G. Scalmani, V. Barone, G. A. Petersson, H. Nakatsuji, X. Li, M. Caricato, A. V. Marenich, J. Bloino, B. G. Janesko, R. Gomperts, B. Mennucci, H. P. Hratchian, J. V. Ortiz, A. F. Izmaylov, J. L. Sonnenberg, Williams, F. Ding, F. Lipparini, F. Egidi, J. Goings, B. Peng, A. Petrone, T. Henderson, D. Ranasinghe, V. G. Zakrzewski, J. Gao, N. Rega, G. Zheng, W. Liang, M. Hada, M. Ehara, K. Toyota, R. Fukuda, J. Hasegawa, M. Ishida, T. Nakajima, Y. Honda, O. Kitao, H. Nakai, T. Vreven, K. Throssell, J. A. Montgomery Jr, J. E. Peralta, F. Ogliaro, M. J. Bearpark, J. J. Heyd, E. N. Brothers, K. N. Kudin, V. N. Staroverov, T. A. Keith, R. Kobayashi, J. Normand, K. Raghavachari, A. P. Rendell, J. C. Burant, S. S. Iyengar, J. Tomasi, M. Cossi, J. M. Millam, M. Klene, C. Adamo, R. Cammi, J. W. Ochterski, R. L. Martin, K. Morokuma, O. Farkas, J. B. Foresman and D. J. Fox, *Gaussian 16 Rev. C.01*, 2016.
35 D. Roy, T. Keith and J. Millam, *GaussView 6.0. 16*, Semichem Inc., Shawnee Mission, 2016, pp. 143–150.
36 T. Sander, J. Freyss, M. von Korff and C. Rufener, *J. Chem. Inf. Model.*, 2015, **55**, 460–473.
37 Molinspiration Cheminformatics free web services, **https://www.molinspiration.com**.
38 Y. Zhang, L. Meng, B. Li, H. Tan, Q. Y. Lin, D. Cheng and H. Shi, *Chem. Biol. Drug Des.*, 2019, **93**, 447–453.
39 H.-T. Kuo, J. Pan, Z. Zhang, J. Lau, H. Merkens, C. Zhang, N. Colpo, K.-S. Lin and F. Bénard, *Mol. Pharm.*, 2018, **15**, 3502–3511.
40 E. Mamlins, L. Scharbert, J. Cardinale, M. Krotov, E. Winter, H. Rathke, B. Strodel, A. O. Ankrah, M. Sathekge and U. Haberkorn, *Mol. Imaging Biol.*, 2023, 1–9.
41 G. Ferro-Flores, M. Luna-Gutiérrez, B. Ocampo-García, C. Santos-Cuevas, E. Azorín-Vega, N. Jiménez-Mancilla, E. Orocio-Rodríguez, J. Davanzo and F. O. García-Pérez, *Nucl. Med. Biol.*, 2017, **48**, 36–44.
42 J. B. Ćwikła and M. Roslan, *pharmaceuticals*, 2021, **14**, 1107.